The Cryosphere Discuss., 9, 2167–2200, 2015
www.the-cryosphere-discuss.net/9/2167/2015/
doi:10.5194/tcd-9-2167-2015

The Cryosphere Discussions
Open Access

Lead detection in Arctic sea ice from CryoSat-2: quality assessment, lead area fraction and width distribution

A. Wernecke and L. Kaleschke

Institute of Oceanography, University of Hamburg, Bundesstrasse 53,
20146 Hamburg, Germany

Received: 26 February 2015 – Accepted: 14 March 2015 – Published: 30 March 2015

Correspondence to: A. Wernecke (andreas.wernecke@uni-hamburg.de)

Published by Copernicus Publications on behalf of the European Geosciences Union.

Abstract

Leads cover only a small fraction of the Arctic sea ice but they have a dominant effect on the turbulent exchange between the ocean and the atmosphere. A supervised classification of CryoSat-2 measurements is performed by a combination with visual MODIS scenes. For several parameters thresholds are optimized and tested in order to reproduce this prior classification. The maximum power of the waveform shows the best classification properties amongst them, including the Pulse Peakiness. With the same correct lead detection rates as of published classifiers, the amount of ice being detected as lead can be reduced by up to 40 %. Lead area fraction estimates based on CryoSat-2 show a major fracturing event in the Beaufort Sea in 2013. The resulting Arctic wide lead width distribution follows a power law with an exponent of 2.47 ± 0.04 for the winter seasons from 2011 to 2014, confirming and complementing a regional study based on a high resolution SPOT image.

1 Introduction

Sea ice modulates all interaction between ocean and atmosphere, namely heat, mass and momentum transports in ice covered regions. It is strongly reducing most of these transports and thereby leaving these processes basically to openings in the ice. These openings, called leads, appear even in regions which are typically covered by thick ice, like the central Arctic. Shear and divergence in the ice cover create new leads (Miles and Barry, 1998). Those areas can exhibit huge temperature differences between cold air and relative warm water. The resulting heat loss causes fast formation of new ice. Even leads covered by thin ice show much higher heat fluxes than the surrounding thick ice (Maykut, 1978). The low albedo of leads promotes an energy flow in the opposite direction which increases the amount of absorbed insolation, resulting in a warming of the underlying water. Leads reduce the internal strength of the sea ice, enabling higher

TCD
9, 2167–2200, 2015

drifting velocities (Rampal et al., 2009) and are expected to influence the atmospheric boundary layer chemistry (e.g. Moore et al., 2014).

Large scale satellite remote sensing studies of lead occurrences have been done based on visual and thermal imagers (e.g. Lindsay and Rothrock, 1995; Willmes and Heinemann, 2015). They are generally limited by the resolution of thermal infrared measurements of about one kilometer and by the influence of clouds. By using passive microwave data, Röhrs et al. (2012) avoided the requirement of free sky conditions but reduced the resolution even further to 6.25 km. A good agreement with CryoSat-2 (CS-2) and ASAR based estimates of the lead occurrence for leads wider than 3 km has been reported (Röhrs et al., 2012). CryoSat-2 based lead detection is expected to be a good complement to previous estimates as it combines an increased resolution of some hundred meters with a strong atmospheric independence. The quality of this approach has been assessed by Zygmuntowska et al. (2013) for airborne surveys and is topic of this study for CS-2 measurements.

Not only the lead area but also the width distribution is important for the turbulent heat transport in ice covered regions. A convective boundary layer evolves over leads which increases in thickness towards the downwind side of the lead. This boundary layer is dampening the heat flux per lead area which is therefore higher for narrow leads than for wider ones. This has led to different lead-width dependent heat transfer formulations (e.g. Andreas and Murphy, 1986). Marcq and Weiss (2012) show that the turbulent heat flux over leads is up to 55 % higher if using a power-law distribution down to a lead width of 10 m instead of considering all leads as one large area of open water.

The Arctic sea ice extent declined substantially over the last decades (Serreze et al., 2007), while comparable studies for the ice thickness are rare and struggle with uncertainties (Lindsay and Schweiger, 2015). Ice thickness estimates based on upward looking sonars on submarines (e.g. Rothrock et al., 2008) or moorings (Proshutinsky et al., 2009) have a relatively sparse temporal and spatial coverage. Airborne and helicopter based thickness measurements are utilizing the strong difference between the electromagnetic inductances of seawater and ice. They are of great value for regional

TCD
9, 2167–2200, 2015

studies and validation, but are limited to individual campaigns (Haas et al., 2010; Renner et al., 2013; Maaß et al., 2015).

Sea ice thickness is retrieved from satellites by radiometry, i.e. the influence of the ice thickness, salinity and temperature on the emissivity and transmittance. Various passive thermal to microwave sensors have been used (AVHRR, MODIS, SSM/I, AMSR-E, MIRAS) (Yu and Rothrock, 1996; Singh et al., 2011; Martin et al., 2005; Kaleschke et al., 2012; Tian-Kunze et al., 2014). As the ice thickness information saturates for all these sensors at a certain level, this approach is only capable of relatively thin ice, typically well below one meter (e.g. Kaleschke et al., 2010).

Another approach utilizes laser or radar altimetry in order to derive the freeboard, i.e. the elevation difference between the Sea Surface Height (SSH) and snow or ice surface. By considering the relevant densities and the snow thickness the freeboard can be converted into an ice thickness in hydrostatic equilibrium. Sea ice thickness has been derived from radar altimetry in the K_u band from the European Remote Sensing Satellites ERS-1 and ERS-2 as well as Envisat and CS-2 (Laxon et al., 2003; Giles et al., 2008; Laxon et al., 2013; Ricker et al., 2014). These radars are not restricted to clear sky conditions, but a satisfying handle for the influence of a snow cover on the signal is still not found (Willatt et al., 2011; Kwok, 2014). Advantages of the radar on CS-2, over earlier K_u band altimeters are the reduced footprint size and noise due to the synthesis of overlapping measurements, its orbit which allows a coverage up to 88° North and South and the potential of interferometric measurements (Wingham et al., 2006).

A crucial information for each altimeter based ice thickness retrieval is the SSH. For this reason the altimeter measurements are separated into those from ice and those from leads (see Fig. 1 for examples from CS-2). The lead measurements are used to derive the SSH, which acts as reference for the freeboard. Leads covered by thin ice and falsely detected leads (i.e. thick ice) result in an overestimation of the SSH and therefore in a negative bias in the derived freeboard and thickness. If considering only a very few, assured lead measurements the statistical error increases (Armitage and

TCD
9, 2167–2200, 2015

Davidson, 2014). It is therefore of high interest to find a lead detection method which is very trustworthy and detects as many leads as possible.

In this study the quality of CS-2 based lead detection procedures is assessed by a comparison with MODIS measurements. Previously published classifiers are implemented and compared with newly derived ones in a Receiver Operating Characteristics (ROC) graph. The most promising one is subsequently used to derive the lead area fraction and the lead width distribution. Thereby this study attempts to close a gap of knowledge about the differences of lead detection procedures from CS-2 and makes suggestions for improvements, which has direct implications for sea ice thickness estimates.

2 Methods

2.1 The ground truth

In order to optimize and compare the performance of different classification routines, we choose a supervised classification approach. The MODIS band 2 swath product is used as reference data as it has a sufficient resolution of 250 m and seems to be even more suited to identify leads than band 1 (not shown). Dark areas with sharp edges and linear shapes in the MODIS images are interpreted as leads. CS-2 measurements from this areas, recorded less than one hour before or after the MODIS acquisition, are manually labeled as lead. In the same way we identify CS-2 measurements of ice while all measurements with a mixture of both classes within the footprint are excluded from this study (see also Fig. 2a). This information is in the following considered as ground truth, regardless of possible mislabeling for example caused by unexpected high ice velocities. The ground truth consists 722 lead and 5768 ice measurements acquired from February to end of April in 2012 and 2013 from seven MODIS granules. For this time of the year optical MODIS scenes are available and surface melting can be ruled out. Within this study we use CryoSat-2 Level 1b data with processor ver-

TCD
9, 2167–2200, 2015

sions “SIR1SAR/4.0” and “SIR1SAR/4.1” (Baseline B). This two SAR mode versions are equivalent.

2.2 Relation to physical properties

When the emitted CS-2 signal reaches a rough surface the elevation differences result in a spread in time of the received signal. Especially if the roughness is close to the signal wavelength of 2.2 cm in K_u band it is favoring surface scattering instead of reflection, resulting in a more uniform distribution in terms of angle dependency. Therefore measurements of the same position from altering look angles are more similar for rough surfaces. Additionally areas further away from the nadir point have a stronger contribution, leading to an emphasized signal following the first (nadir) peak for rough surfaces. As the emitted power is more strongly scattered in all directions, the maximal receivable signal is reduced.

The characteristic impedance of the surface layer might also influence the signal. If the difference in impedance at 13.5 GHz of the uppermost layer and the air is small, there is less reflection and more transmission into the ice/snow. Within the medium it is partly absorbed and scattered by inhomogeneities, again leading to a spread of the signal with lower maximum values and a more homogeneous angular distribution. This process could for example be favored by a layer of wet snow.

As leads are locally bound, the fetch is too small for bigger waves to evolve in the water. The thin ice cover, if present, is yet neither physically deformed nor covered with snow. Furthermore the microstructure of young ice is more compact than of older ice as most brine pockets are filled and less connections have evolved. Therefore leads can be characterized by their commonly flat surface with relatively high impedance difference to the air. The returns originating from leads are expected to be compressed in time with higher maximum values and stronger incidence angle dependency (specular returns).

In the SAR Mode, CS-2 returns from the same position on the ground are received from different look angles. After allocating them by using the Doppler Shift, they are

TCD
9, 2167–2200, 2015

combined to one waveform i.e. the returned power as function of time (see Fig. 1 for examples). The following waveform based parameters are used: Maximum Power, Pulse Peakiness, Leading Edge Width and Trailing Edge Width.

In addition to stacking the beams to one waveform, they are also integrated over time separately. In this case the returned energy of the individual beams (the stack) with different incidence angles is achieved. We use the Stack Standard Deviation and the Stack Kurtosis as stack based parameters.

2.3 Parameter definition

- The Maximum Power (MAX) is the highest recorded power of the calibrated waveform in Watts.

- The Pulse Peakiness (PP) has been established by Laxon (1994) and is defined as the MAX divided by the accumulated power (P^{WF}) of all bins constituting the waveform:

$$\mathrm{PP} = \frac{\max\left(P^{\mathrm{WF}}\right)}{\sum_{i=1}^{128} P_i^{\mathrm{WF}}}, \tag{1}$$

  which is the same definition as used by Armitage and Davidson (2014), while the values of Laxon et al. (2013) are divided by 100 and those of Ricker et al. (2014) by 128 for consistency.

- The Left and Right Pulse Peakiness (PPL and PPR) from Ricker et al. (2014) for Baseline B data are defined as (Robert Ricker, personal communication, January 2015):

TCD
9, 2167–2200, 2015

$$\mathrm{PPL} = \frac{15 \cdot \max\left(P^{\mathrm{WF}}\right)}{\sum_{i=imax-6}^{imax-2} P_i^{\mathrm{WF}}}, \quad (2)$$

$$\mathrm{PPR} = \frac{15 \cdot \max\left(P^{\mathrm{WF}}\right)}{\sum_{i=imax+2}^{imax+6} P_i^{\mathrm{WF}}}, \quad (3)$$

where *i*max is the index of the maximal value of the waveform. The PPL and PPR are proposed in order to reject off-nadir leads which are, based on our methodology (see Sect. 2.1), not expected to appear in our data. Therefore the PPL and PPR are not fully included in this study. However, they are defined as we use the classifier of Ricker et al. (2014) for comparisons.

- The Leading Edge Width (LEW) is defined as the width between 1 and 99 % of the amplitude of a Gaussian fit to the leading edge of the waveform. The fitted area starts at the first bin reaching one percent of the Maximum Power and ends at the second bin, following the first peak. The first peak is the first local maximum reaching at least 50 % of the Maximum Power. To avoid bimodal waveforms, we completely exclude measurements with a first peak smaller than 80 % of the Maximum Power from this study. Similar fits and constrains are used by Kurtz et al. (2014).

- The Trailing Edge Width (TEW) is defined as the width between 99 and 1 % of the amplitude of an exponentially decaying fit to the trailing edge of the waveform. The fitted area starts at the position of the Maximum Power and ends at the last bin (e.g. Legresy et al., 2005).

- The Stack Standard Deviation (SSD) is the standard deviation (SD) a random variable would have, if the Gaussian fit to the integrated power (i.e. energy) as

TCD
9, 2167–2200, 2015

function of beams would be its Probability Density Function. It is therefore describing its width and not the SD of the energy values itself. The used unit is "Beams" which can also be expressed in terms of angles (Wingham et al., 2006).

– The Stack Kurtosis (SK) is also obtained from the Gaussian fit to the energy as function of beams. In contrast to the SSD it is not derived as a fitting variable but from the function, evaluated at the positions of the beams (Veit Helm, personal communication, June 2014; Wingham et al., 2006). While all Gaussian functions have in general a kurtosis of three, discrete points of them do not have if the Gaussian is badly represented. This is the case for very narrow (badly resolved) and extremely wide functions (only partly covered).

2.4 Threshold optimization

Threshold based classifications are widely used to identify leads from K_u band altimeters. We use a repeated random sub-sampling validation technique to derive and test thresholds ($\boldsymbol{\Theta}$). This involves a random separation of the samples into a training and a testing subset, each of which consist of 50 % of all samples. From the training subset we derive $\boldsymbol{\Theta}$ and apply it to the testing set to investigate its performance. The random assignment into subsets and the testing of the newly derived $\boldsymbol{\Theta}$ is repeated 200 times to get an overall performance and an estimation of its spread.

As mentioned in Sect. 1 there are different applications for lead detection algorithms also resulting in different demands on its characteristics. One plausible aim is to reduce the total amount of false detections to a minimum. But one might also be interested in a more conservative lead detection by reducing the amount of ice being detected as lead (False Leads) at the cost of less correctly detected leads (True Leads). A more conservative detection might be used for a freeboard retrieval as False Leads might result in a bias while high True Lead Rates are not always of high importance.

TCD
9, 2167–2200, 2015

To take these different demands into account we include a weighting factor w in the cost function.

$$\text{cost}(\boldsymbol{\Theta}) = w \cdot \text{False\_Ice}(\boldsymbol{\Theta}) + \text{False\_Leads}(\boldsymbol{\Theta}), \quad (4)$$

where False_Ice represents the amount of lead samples classified as ice. $\boldsymbol{\Theta}$ is derived by minimizing the cost function on the training subset using the Nelder–Mead simplex algorithm with up to 400 initial guesses to find the global minimum. For $0 < w < 1$ False Leads are primarily reduced, while for $w = 1$ the total amount of false classifications is minimized. We use the parameter acronym with the weight as index to point at the corresponding one dimensional classifier.

This methodology is applied to all single parameters and all possible pairs of them, in the latter case forming two dimensional feature spaces.

3 Results

3.1 Classification performance

In Fig. 2 the CS-2 track is essentially crossing three wider leads, two of which are brighter at the northern side. This indicates that they are covered by ice on this side, while the southern side might exhibit open water. The third wider lead around 71.2° N and a thinner one at 71.75° N seem both to be completely covered by thin ice. The manual classification in Fig. 2a only visualizes the methodology as the time difference is larger than one hour and this scene is therefore not part of the ground truth. Gaps in the track occur when the MODIS information of CS-2 footprints cannot be assigned unambiguously to leads or ice. In Fig. 2b the $\text{MAX}_{0.5}$ classifier detects only some leads and those only partly. It shows an accentuation on newly formed parts of the leads. The MAX_1 classifier and the one developed by Ricker et al. (2014) show strong similarities as both detect all relevant leads while lead detections are very rare where the MODIS scene shows ice. However for wider leads they can show a mixture of ice and lead

TCD
9, 2167–2200, 2015

detections, which is in some cases stronger for the MAX_1 classifier and in other cases for the Ricker et al. (2014) classifier (not shown). The classifier from Laxon et al. (2013) detects all visible leads without a significant amount of missing lead detections, but it also detects leads where no or only weak indications for them can be found in the MODIS scene.

Figure 3 shows a Receiver Operating Characteristics (ROC) graph of all tested classifiers. Each classifier is represented by one point in the graph, the position of which is defined by its True Lead Rate (TLR, the amount of correctly detected leads divided by the amount of tested lead samples) and False Lead Rate (FLR, the amount of ice measurements detected as lead divided by the amount of tested ice samples). The upper left corner corresponds to ideal classifiers and the principle diagonal represents random assignments. For each parameter and pairs of them, we use different weights resulting in different $\boldsymbol{\Theta}$ and corresponding performances. For single parameter classifiers 15 different weights (0.001, 0.1, 0.2, 0.3, 0.4, 0.5, 0.6, 0.7, 0.8, 1, 2, 5, 10, 30, 100) are applied to capture the development of the performance (from the lower left corner to the upper right in Fig. 3) while $w = 0.001$, $w = 0.5$ and $w = 1$ are used in the two dimensional case. To follow the performance of e.g. MAX based classifiers one can start with small w, implying high values of Θ which is detecting only a few leads (lower left corner in Fig. 3). With increasing w and decreasing Θ the TLR increases in the beginning much faster than the FLR. At some point the amount of correct lead detections is mostly constant while a further lowering of Θ is mainly increasing the amount of ice measurements which are detected as lead. As relative performances are shown the classifier closest to the upper left corner is not necessarily the "best" one but if one classifier is on the upper left side of another it can be considered as superior. Further remarks on ROC graphs are given by Fawcett (2006).

It is at this point not important how the thresholds ($\boldsymbol{\Theta}$) are derived but only the combination of its value and performance. This allows us to compare the classifiers found here with those other authors have developed, independent from the optimization routine.

TCD
9, 2167–2200, 2015

Classifiers based on the Maximum Power (MAX) appear on the upper left side of all others on the whole range of Fig. 3. Only classifiers using two parameters including the MAX (black marker) reach the single feature MAX classifications and are in all cases very close to them. All other classifiers based on pairs also show very similar results to that classifier based on the single, more suited parameter within its pair.

The PP and LEW based classifiers show strong similarities and have the second-best combinations of True and False Lead Rates.

Figure 4a illustrates the spread within the runs in terms of the SD of the True and False Lead Rates. The differences between all shown one dimensional classifiers and the corresponding two dimensional ones are clearly smaller than the inherent fluctuations and are therefore considered as not significant. The classifiers based on the MAX are separated from the others by more than their SDs for small weights, while they are not for higher weights. However, Fig. 4b shows that the fluctuations occur mostly in the direction of neighboring weights, which shows that the performance of MAX based classifiers is even stronger separated from the others.

3.2 Spatial distribution

In the following sections we are using the MAX_1 classifier which has been derived by minimizing the total amount of false classifications and its results are therefore taken as the best representation of the overall lead occurrence.

Figure 5 shows the lead fraction in the Arctic region as derived from CS-2 by dividing the amount of detected lead measurements by the total amount of measurements from January to March 2011. The AMSR-E Arctic lead area fraction (Röhrs and Kaleschke, 2012; Röhrs et al., 2012) (downloaded in September 2014) is also shown, combined over the same period and brought to the same spatial resolution.

Lead detections from CS-2 are most common in the Baffin Bay, the Fram Strait region, the northern Barents Sea and the Kara Sea, as well as in the Laptev and the Chukchi Sea, all with lead fractions up to around 15 % (Fig. 5a). The central Arctic including the area north of the Canadian Arctic Archipelago and the northern Canada

TCD
9, 2167–2200, 2015

Basin show low lead fractions of around 0–1.5 %. In the southern Beaufort sea and especially its shear zone next to the coast line, lead fraction values of up to 6 % occur.

A somewhat different picture of the lead fraction pattern emerges by using the AMSR-E Arctic lead area fraction from Röhrs et al. (2012) (Fig. 5b). In areas covered by both estimates the CS-2 based one mostly appears to be higher than the AMSR-E based estimate. This is not the case in the south eastern Beaufort sea where the AMSR-E product shows values of 15 % and more while they reach from 1.5 to 5 % for the CS-2 based estimate. We observe reasonable agreements in the Fram Strait region, the East Siberian Sea and the Chukchi Sea. Increased values occur for both estimates near islands like Svalbard, Franz Josef Land, Severnaya Zemlya and the Wrangel Island. However there are big differences between the datasets in the Baffin Bay, the Fram Strait regions close to the ice edge, the northern Barents Sea and the Kara Sea where CS-2 consistently detects more leads than the AMSR-E lead area fraction indicates.

While a daily open ocean mask is provided for the AMSR-E product, we consider all areas north of 65° N for the CS-2 based estimates. The ice edge on the Atlantic side, as indicated by the AMSR-E mask agrees well with the transition of CS-2 lead fractions from zero to higher values.

By the end of February 2013 the whole Beaufort Sea was pervaded by leads. Favored by storms the ice started in mid February to move into the direction of the Bering Strait, causing a divergence in the pack ice. This is the reason for the opening of leads, beginning in the western part and propagating to the east. This process accelerated around 27 February after which all but the fast ice at the Canadian coast and the sea ice at the Canadian Arctic Archipelago was fractured. See also Beitsch et al. (2014) for further descriptions.

By comparing the CS-2 lead fractions from February and March 2013 (Fig. 6) the pattern of this fracture event are reproduced with a proper shape and amplitude. Most lead pattern can be observed in both months, in many cases slightly decreasing in amplitude towards March. However, while in February only in the western part of the

TCD
9, 2167–2200, 2015

Beaufort Sea noticeable amounts of leads are detected, the complete region shows 8 to 15 % lead coverage in March.

3.3 Apparent lead width

To investigate the lead width distribution we use a proxy which we call apparent lead width. The apparent lead width is the amount of consecutive MAX_1 lead detections multiplied by the approximate distance between two positions of 300 m. It can be seen as a measure of the CS-2 track interval over a crossed lead or as the width of a lead how it appears in the one dimensional domain of the CS-2 track. If the lead orientation is orthogonal to the CS-2 track, the apparent lead width is our best estimate of the actual lead width. We do not allow any ice detection within a lead which will in case of false detections split a lead into smaller ones.

The apparent lead width distribution follows a power-law in winter months with an exponent of 2.47 for values of 600 m and more (Fig. 7). A quantity z is called power-law distributed if its Probability Density Function $p(z)$ satisfies:

$$p(z) \propto z^{-a}, \tag{5}$$

where a is the power-law exponent. It is derived following the approximation of Clauset et al. (2009) for discrete distributions with a simple adjustment for a step size of 300 m as shown in Eq. (6).

$$a \approx 1 + N_Z \left(\sum_{i=1}^{N_Z} \ln \frac{z_i}{z_{\min} - \frac{1}{2} \cdot 300\,\mathrm{m}} \right)^{-1} \tag{6}$$

For the calculation of the power-law exponent only apparent lead widths z_i with a width equal or higher than $z_{\min} = 900$ m are considered with N_Z being the amount of them. A line representing a power-law with the calculated exponent is displayed in Fig. 7. It shows the validity of this approximation down to 600 m, as both lines show a strongly parallel development.

TCD
9, 2167–2200, 2015

The interannual variability is small with exponents between 2.42 in 2013 and 2.52 in 2011 with a SD of 0.04 amongst all four years. Differences between January, February and March of the same year are even smaller while the exponent decreases towards spring and autumn. All calculated distributions are following a power-law for apparent lead widths of 600 m and more.

4 Discussion

4.1 Classification performances

Classifiers based on the MAX parameter show generally the best ratio between correctly detected leads and ice being falsely detected as lead. A classifier using MAX $> 2.58 \times 10^{-11}$ W as threshold (MAX_1) detects 68.18 % of all leads correctly while only 3.41 % of the tested ice measurements are detected as leads. The PP_1 classifier using 0.35 as threshold has a TLR of 64.66 % (instead of 68.18 %) and a FLR of 4.09 % (instead of 3.41 %). The differences are even stronger for higher thresholds of 1.22×10^{-10} W and 0.425, respectively ($MAX_{0.5}$ and $PP_{0.5}$, Table 1).

The performances of individual runs overlap only slightly for $w = 1$ and are well separated for $w = 0.5$. This shows that the performance improvement is significant. The increased fluctuation in the direction of neighboring weights in Fig. 4b is likely to be caused by a variability of the thresholds caused by the repeated optimization.

For airborne surveys with an device very similar to SIRAL on CS-2, Zygmuntowska et al. (2013) also found the MAX parameter to have less false lead classifications than all other parameters. The best combination of parameters (MAX & TEW) with an Bayesian classifier improves its rate only little from 6.5 to 6.2 %. Zygmuntowska et al. (2013) define the False Lead Classification Rate (FLCR) as percentage of all lead detections originating from sea ice. This is different to our False Lead Rate as we use the amount of true ice measurements as base. The FLCR calculated from the absolute values in Table 1 are 28.6 and 12.5 % for the MAX_1 and $MAX_{0.5}$ classifier, respectively.

TCD
9, 2167–2200, 2015

One reason for higher error rates of CS-2 is the reduced resolution of 300 m × 1500 m in contrast to around 10 m × 50 m for the airborne device. Thereby it becomes much more likely that different surface types occur within one footprint. Further we have to allow for some temporal differences in the data acquisition and have to collocate the datasets, while for the airborne surveys optical images are taken simultaneously. Deficiencies of the ground truth increase the error rates which might be overestimated. However, as this effects all parameters it is likely that the influence on the comparison is small.

Compared to their MAX classifier, the PP classifier of Zygmuntowska et al. (2013) is detecting more leads from both, ice and lead measurements. This is directly connected to applied thresholds and is not a parameter property. For a solid decision which parameter is suited best for lead detection it is necessary to vary the thresholds. We are able to propose the use of the MAX parameter instead of the PP.

Three classifiers developed by other authors are included in this study. With the same amount of False Lead detections, the True Lead Rates can be increased for our dataset from 9 to ∼ 13 % (Röhrs et al., 2012), from 83 to ∼ 89 % (Laxon et al., 2013) or from 61 to ∼ 79 % (Ricker et al., 2014) if an optimized threshold of the MAX parameter is used instead. On the other hand the False Lead Rate can be reduced for a constant True Lead Rate from 13 to ∼ 7 % (−38 %) or from 5 to ∼ 3 % (−40 %) for the Laxon et al. (2013) and Ricker et al. (2014) classifier, respectively (Fig. 3).

So far we defined a lead detection as a measurement reaching both thresholds, but the same procedure has been performed by taking it as sufficient to reach only one of them. This results in more demanding thresholds but like before in no improvement of the classification (not shown). There seems to be no benefit in including a second feature, because of which the optimization shifts the second threshold to some level where it does not harm. The lack of improvement indicates that the parameters are basically all utilizing the same physical information and that the instrument and fading noises have either an correlated influence on all parameters or the influence is not significant at all. As some of the parameters are derived in a very different way, firstly by stacking different beams and secondly by integrating them over time separately, we

TCD
9, 2167–2200, 2015

do not expect the noise to affect them in the same way. We further conclude that the spread of the parameters within one class is predominantly caused by variations of surface properties which produces a correlation of all parameters.

4.2 Off-nadir leads

Due to the high amplitude of returns from leads it is possible that leads which are not directly in nadir direction are dominating the signal. As this can cause a bias in elevation estimates Ricker et al. (2014) introduced the Left and Right Pulse Peakiness to avoid off-nadir leads. It has further been shown that it is, to some extent, possible to reduce the influence of off-nadir leads by increasing the Pulse Peakiness threshold of a single parameter classifier (Armitage and Davidson, 2014). This is done at the cost of discarding ~ 60 % of the lead detections and thereby increasing the statistical error. The underlying process allowing for this reduction is the influence of the surface orientation towards the sensor on the maximum return. The relative orientation, favoring high maximum values the most, is expected to be found close to the nadir point. The further away from this point the main scattering surface (i.e. the lead) is, the more power is reflected away from the sensor instead of back towards it. This process is influencing the MAX value in the first place which has then implications for the PP (Armitage and Davidson, 2014). Therefore it is reasonable to assume that the influence of off-nadir leads is also reduced for high MAX thresholds, potentially even stronger than for the PP as the process causing this reduction has a more direct impact on it.

4.3 Spatial distribution

The CS-2 lead fraction shows a reasonable spatial distribution. It is small in the central Arctic and north of the Canadian Arctic Archipelago which are typical regions of thick multi-year ice. It shows high values in regions of high drifting velocities or known to favor the development of polynyas like the Fram Strait, the Laptev Sea and the Chukchi Sea. The lead fractions are also increasing around most islands and coasts which

TCD
9, 2167–2200, 2015

introduce shear between the land fast ice and the drifting pack ice. The absolute lead fraction values tend to be higher but are mostly in agreement with those of Lindsay and Rothrock (1995). They found lead fractions of 2 to 3 % for the central arctic and 6 to 9 % in the peripheral seas in the winter using the Advanced Very High Resolution Radiometer (AVHRR).

In nearly all regions the CS-2 lead fraction exceeds the AMSR-E Arctic lead area fraction from Röhrs et al. (2012) (Fig. 5). While the AMSR-E product only detects most leads with a width of 3 km and more, a width of some hundred meters is sufficient for detection by CS-2. As shown in Sect. 3.3 the apparent lead width is following a power law on the scale of kilometers, implying that measurements from narrow leads are largely outnumbering those from wider leads. In contrast to the CS-2 lead fraction, the AMSR-E product is additionally not including very large regions of thin ice like huge polynyas as a spatial high-pass filter is used.

The ice edge towards the North Atlantic is captured by both approaches quite similar. We expect the ice edge to be at the interface between areas of no lead detections around the Norwegian and central Barents Sea and neighboring areas of higher lead fractions in Fig. 5a. This allows the inference that the MAX_1 classifier detects no leads over the open ocean. For this reason grid cells at the very ice edge are likely to underestimate the lead fraction relative to the ice covered part of the cell.

While the AMSR-E lead fraction drops relative consistently down to values around 2–3 % within a belt of around 200 km from the ice edge, CS-2 based estimates show much higher values of around 12 % in this areas. The high values in the marginal ice zone are reasonable as this area is likely to be fractured due to the influence of ocean waves. Especially in the Baffin Bay, the northern Barents Sea and the Kara Sea high rates of new ice formation can occur in winter which is in good agreement with high CS-2 lead fractions of these regions. The general reasonable distribution and its alternation increase our confidence in our lead detection algorithm.

TCD
9, 2167–2200, 2015

4.4 Apparent lead width

Compared to the power-law, the found number of apparent lead width of 300 m is smaller than expected. This is a typical feature on the lower bound of the resolution as leads of this size are not always covered by a single measurement but partially by more, not necessarily leading to a detection. This is intensified by the elongated footprint of CS-2 as small leads may only be detected if they cover most of the width of the footprint. Therefore it is likely that the bend on the lower bound of the distribution in Fig. 7 is induced by the measurement characteristics and not by the actual lead distribution.

Marcq and Weiss (2012) have found a power-law exponent similar to our between 2.1 and 2.6 for scales from 20 m to 2 km by analyzing a single SPOT image with a resolution of 10 m. In two submarine based surveys, power-laws with exponents of 2 and 2.29 were found for the regions from the Fram Strait to the North Pole and the Davis Strait, respectively (Wadhams, 1981; Wadhams et al., 1985). In both cases resolutions of about 5 m are present and the power-law holds for the range from 50 to 1000 m. The examination of submarine and mooring data by Kwok et al. (2009) also indicates a strong accumulation of lead widths down to 5 m but the distribution has not been analyzed. For the central Arctic, a study of Lindsay and Rothrock (1995) also states a power-law distribution, but with a mean exponent of 1.6 for scales from one to around 50 km. It is based on thermal to near visible infrared measurements from the AVHRR, which is despite its resolution of one kilometer expected to detect leads with a minimum width below this size. It has been discussed whether the lead width distribution might be scale dependent (Lindsay and Rothrock, 1995; Marcq and Weiss, 2012) which seems not to be the case, as we found a stable power-law behavior on scales partly covering those of all other studies.

The results of Lindsay and Rothrock (1995) are contradictory to ours as we found a higher power-law exponent, implying a higher fraction of narrow leads. One explanation would be the relative coarse resolution of the AVHRR in combination with its high

TCD
9, 2167–2200, 2015

sensitivity to leads. This could cause leads to appear wider then they are, as well as several narrow ones to appear as one wide lead, resulting in a less steep apparent lead width distribution. Comparisons with MODIS images indicate that the classifier used in this study switches in some cases between lead and ice detections over refrozen leads. This could result in an overestimation of the power-low exponent. The estimates might also have a different tolerance of refrozen leads, while both include at least the early stages of freezing. The size of leads is often growing with time as the surrounding ice floes keep drifting apart, meaning that estimates which include older leads are also likely to show less steep apparent lead width distributions.

Another reason could be an actual shift in the distribution between the periods from 1989 to 1995 and 2011 to 2014. This would be consistent with the results of Marcq and Weiss (2012) but would not explain the differences to those studies by Wadhams (1981) and Wadhams et al. (1985). However, this shift could be driven by observed changes in the amount of perennial ice, the ice thickness and drifting velocities (Nghiem et al., 2007; Haas et al., 2008; Rampal et al., 2009). Rampal et al. are further linking a found increase in winter strain rates between 1978 and 2007 to a weakening in mechanical strength of the ice and increased fracturing. We found no sign for a trend of the power-law exponent within the four years of CS-2 data.

4.5 Implications of apparent lead width distribution

A transformation from apparent to actual lead width is not possible without profound knowledge of the sensitivity of lead detections and requires assumptions about the shape and orientation of leads. This is impeded by a nonuniform distribution of lead orientation (Bröhan and Kaleschke, 2014). For most applications it is not necessary to perform this transformation as this is the way leads appear to anything moving along sea ice, including the wind acting on the ocean surface.

The apparent lead width distribution is showing a strong intensification towards smaller lead widths. The area contribution of leads having the width z is $z \cdot p(z) \propto z^{-2.47+1}$, which is still relatively fast decreasing with increasing width. This indicates

TCD
9, 2167–2200, 2015

that every lead area estimate which is not capable of detecting narrow leads is very likely to underestimate the total lead area. For a parametrization of lead area estimates it is of high interest to know down to which bound the power law behavior holds. This defines not only the mean lead width but also the fraction of lead area which is not captured by the estimate.

5 Conclusions

This study presented the potentials of several parameters and combinations of them to distinguish between CryoSat-2 measurements from leads and those from ice. They have been tested by deriving thresholds and analyzing their capabilities of reproducing a prior classification. The combination of parameters, even though common practice, has not shown any advantage for threshold based classifications. Using the maximum value of the waveform has in all cases shown better results than any other tested parameter, including the Pulse Peakiness. Compared to the classifier of Laxon et al. (2013) a threshold of 1.22×10^{-10} W on the MAX detected only half the amount of true leads but was able to reduce the percentage of ice being detected as lead from around 13 to less than 1 %. A solid lead detection, which ensures that nearly all lead classifications are actually originating from leads is the requirement for a precise, unbiased freeboard retrieval. It thereby helps to improve ice thickness estimates, which is one of the major aims of the CryoSat-2 mission.

A lower threshold of 2.58×10^{-11} W was used as the best representation of the overall lead occurrence. It showed reasonable spatial distributions with relatively high lead fractions of around 12 % in the marginal ice zone. The apparent lead width was derived from the amount of consecutive lead detections. Its distributions is following a power-law with exponent of 2.47 ± 0.04 which implies a concentration of both, amount and area contribution at small lead widths. Embedding this work into those of others, a scale independent lead width distribution from 20 m to 50 km is likely. The implications for a parametrization of low resolution lead area estimates were addressed and its de-

TCD
9, 2167–2200, 2015

pendency on the lower bound of the found distribution emphasized. The turbulent heat transport over ice covered regions is known to be strongly lead width dependent on small scales. The found distribution is suggesting that the work of Marcq and Weiss (2012), based on a single SPOT scene, can be generalized. This implies a much higher heat transport per lead area than it would be obtained by wide leads. In this manner the presented findings can help to improve the parameterization of this fundamental process in coupled ocean–ice–atmosphere models.

The Supplement related to this article is available online at doi:10.5194/tcd-9-2167-2015-supplement.

Acknowledgements. This work is supported by the German Federal Ministry of Education and Research (FKZ: 01LP1126A) and in parts through the Cluster of Excellence "CliSAP" (EXC177), University of Hamburg, funded through the German Science Foundation (DFG). CryoSat-2 data are provided by the European Space Agency (ESA). Additionally we would like to acknowledge the use of Rapid Response imagery from the Land Atmosphere Near-real time Capability for EOS (LANCE) system operated by the NASA/GSFC/Earth Science Data and Information System (ESDIS) with funding provided by NASA/HQ. The AMSR-E Arctic lead area fraction is provided by the Integrated Climate Data Center (ICDC, http://icdc.zmaw.de/), University of Hamburg, Hamburg, Germany. We would like to thank Veit Helm, Stefan Hendricks and Robert Ricker for the kind and fruitful discussions.

References

Andreas, E. L. and Murphy, B.: Bulk transfer coefficients for heat and momentum over leads and polynyas, J. Phys. Oceanogr., 16, 1875–1883, 1986. 2169

Armitage, T. W. and Davidson, M. W.: Using the interferometric capabilities of the ESA CryoSat-2 mission to improve the accuracy of sea ice freeboard retrievals, IEEE T. Geosci. Remote, 52, 529–536, 2014. 2170, 2173, 2183

TCD
9, 2167–2200, 2015

Beitsch, A., Kaleschke, L., and Kern, S.: Investigating high-resolution AMSR2 sea ice concentrations during the February 2013 fracture event in the Beaufort Sea, Remote Sens., 6, 3841–3856, 2014. 2179

Bröhan, D. and Kaleschke, L.: A nine-year climatology of Arctic sea ice lead orientation and frequency from AMSR-E, Remote Sens., 6, 1451–1475, 2014. 2186

Clauset, A., Shalizi, C. R., and Newman, M. E.: Power-law distributions in empirical data, SIAM Rev., 51, 661–703, 2009. 2180

Fawcett, T.: An introduction to ROC analysis, Pattern Recogn. Lett., 27, 861–874, 2006. 2177

Giles, K. A., Laxon, S. W., and Ridout, A. L.: Circumpolar thinning of Arctic sea ice following the 2007 record ice extent minimum, Geophys. Res. Lett., 35, L22502, doi:10.1029/2008GL035710, 2008. 2170

Haas, C., Pfaffling, A., Hendricks, S., Rabenstein, L., Etienne, J.-L., and Rigor, I.: Reduced ice thickness in Arctic Transpolar Drift favors rapid ice retreat, Geophys. Res. Lett., 35, L17501, doi:10.1029/2008GL034457, 2008. 2186

Haas, C., Hendricks, S., Eicken, H., and Herber, A.: Synoptic airborne thickness surveys reveal state of Arctic sea ice cover, Geophys. Res. Lett., 37, L09501, doi:10.1029/2010GL042652, 2010. 2170

Kaleschke, L., Maaß, N., Haas, C., Hendricks, S., Heygster, G., and Tonboe, R. T.: A sea-ice thickness retrieval model for 1.4 GHz radiometry and application to airborne measurements over low salinity sea-ice, The Cryosphere, 4, 583–592, doi:10.5194/tc-4-583-2010, 2010. 2170

Kaleschke, L., Tian-Kunze, X., Maaß, N., Mäkynen, M., and Drusch, M.: Sea ice thickness retrieval from SMOS brightness temperatures during the Arctic freeze-up period, Geophys. Res. Lett., 39, L05501, doi:10.1029/2012GL050916, 2012. 2170

Kurtz, N. T., Galin, N., and Studinger, M.: An improved CryoSat-2 sea ice freeboard retrieval algorithm through the use of waveform fitting, The Cryosphere, 8, 1217–1237, doi:10.5194/tc-8-1217-2014, 2014. 2174

Kwok, R.: Simulated effects of a snow layer on retrieval of CryoSat-2 sea ice freeboard, Geophys. Res. Lett., 41, 5014–5020, 2014. 2170

Kwok, R., Cunningham, G., Wensnahan, M., Rigor, I., Zwally, H., and Yi, D.: Thinning and volume loss of the Arctic Ocean sea ice cover: 2003–2008, J. Geophys. Res.-Oceans, 114, C07005, doi:10.1029/2009JC005312, 2009. 2185

TCD
9, 2167–2200, 2015

Laxon, S. W.: Sea ice extent mapping using the ERS-1 radar altimeter, EARSeL Adv. Remote Sens., 3, 112–116, 1994. 2173
Laxon, S. W., Peacock, N., and Smith, D.: High interannual variability of sea ice thickness in the Arctic region, Nature, 425, 947–950, 2003. 2170
Laxon, S. W., Giles, K. A., Ridout, A. L., Wingham, D. J., Willatt, R., Cullen, R., Kwok, R., Schweiger, A., Zhang, J., Haas, C., Hendricks, S., Krishfield, R., Kurtz, N., Farrell, S. and Davidson, M.: CryoSat-2 estimates of Arctic sea ice thickness and volume, Geophys. Res. Lett., 40, 732–737, 2013. 2170, 2173, 2177, 2182, 2187, 2193, 2195
Legresy, B., Papa, F., Remy, F., Vinay, G., van den Bosch, M., and Zanife, O.-Z.: ENVISAT radar altimeter measurements over continental surfaces and ice caps using the ICE-2 retracking algorithm, Remote Sens. Environ., 95, 150–163, 2005. 2174
Lindsay, R. and Rothrock, D.: Arctic sea ice leads from advanced very high resolution radiometer images, J. Geophys. Res.-Oceans, 100, 4533–4544, 1995. 2169, 2184, 2185
Lindsay, R. and Schweiger, A.: Arctic sea ice thickness loss determined using subsurface, aircraft, and satellite observations, The Cryosphere, 9, 269–283, doi:10.5194/tc-9-269-2015, 2015. 2169
Maaß, N., Kaleschke, L., Tian-Kunze, X., Mäkynen, M., Drusch, M., Krumpen, T., Hendricks, S., Lensu, M., Haapala, J., and Haas, C.: Validation of SMOS sea ice thickness retrieval in the northern Baltic Sea, Tellus A, 67, 24617, doi:10.3402/tellusa.v67.24617, 2015. 2170
Marcq, S. and Weiss, J.: Influence of sea ice lead-width distribution on turbulent heat transfer between the ocean and the atmosphere, The Cryosphere, 6, 143–156, doi:10.5194/tc-6-143-2012, 2012. 2169, 2185, 2186, 2188
Martin, S., Drucker, R., Kwok, R., and Holt, B.: Improvements in the estimates of ice thickness and production in the Chukchi Sea polynyas derived from AMSR-E, Geophys. Res. Lett., 32, L05505, doi:10.1029/2004GL022013, 2005. 2170
Maykut, G. A.: Energy exchange over young sea ice in the central Arctic, J. Geophys. Res.-Oceans, 83, 3646–3658, 1978. 2168
Miles, M. W. and Barry, R. G.: A 5-year satellite climatology of winter sea ice leads in the western Arctic, J. Geophys. Res.-Oceans, 103, 21723–21734, 1998. 2168
Moore, C. W., Obrist, D., Steffen, A., Staebler, R. M., Douglas, T. A., Richter, A., and Nghiem, S. V.: Convective forcing of mercury and ozone in the Arctic boundary layer induced by leads in sea ice, Nature, 506, 81–84, doi:10.1038/nature12924, 2014. 2169

TCD
9, 2167–2200, 2015

Nghiem, S., Rigor, I., Perovich, D., Clemente-Colon, P., Weatherly, J., and Neumann, G.: Rapid reduction of Arctic perennial sea ice, Geophys. Res. Lett., 34, L19504, doi:10.1029/2007GL031138, 2007. 2186

Proshutinsky, A., Krishfield, R., Timmermans, M.-L., Toole, J., Carmack, E., McLaughlin, F., Williams, W. J., Zimmermann, S., Itoh, M., and Shimada, K.: Beaufort Gyre freshwater reservoir: state and variability from observations, J. Geophys. Res.-Oceans, 114, C00A10, doi:10.1029/2008JC005104, 2009. 2169

Rampal, P., Weiss, J., and Marsan, D.: Positive trend in the mean speed and deformation rate of Arctic sea ice, 1979–2007, J. Geophys. Res.-Oceans, 114, C05013, doi:10.1029/2008JC005066, 2009. 2169, 2186

Renner, A. H. H., Hendricks, S., Gerland, S., Beckers, J., Haas, C., and Krumpen, T.: Large-scale ice thickness distribution of first-year sea ice in spring and summer north of Svalbard, Ann. Glaciol., 54, 13–18, 2013. 2170

Ricker, R., Hendricks, S., Helm, V., Skourup, H., and Davidson, M.: Sensitivity of CryoSat-2 Arctic sea-ice freeboard and thickness on radar-waveform interpretation, The Cryosphere, 8, 1607–1622, doi:10.5194/tc-8-1607-2014, 2014. 2170, 2173, 2174, 2176, 2177, 2182, 2183, 2193, 2195

Röhrs, J. and Kaleschke, L.: An algorithm to detect sea ice leads by using AMSR-E passive microwave imagery, The Cryosphere, 6, 343–352, doi:10.5194/tc-6-343-2012, 2012. 2178

Röhrs, J., Kaleschke, L., Bröhan, D., and Siligam, P. K.: Corrigendum to "An algorithm to detect sea ice leads by using AMSR-E passive microwave imagery" published in The Cryosphere, 6, 343–352, 2012, The Cryosphere, 6, 365–365, doi:10.5194/tc-6-365-2012, 2012. 2169, 2178, 2179, 2182, 2184, 2193, 2195, 2198

Rothrock, D., Percival, D., and Wensnahan, M.: The decline in arctic sea-ice thickness: separating the spatial, annual, and interannual variability in a quarter century of submarine data, J. Geophys. Res.-Oceans, 113, C05003, doi:10.1029/2007JC004252, 2008. 2169

Serreze, M. C., Holland, M. M., and Stroeve, J.: Perspectives on the Arctic's shrinking sea-ice cover, Science, 315, 1533–1536, 2007. 2169

Singh, R. K., Oza, S. R., Vyas, N. K., and Sarkar, A.: Estimation of thin ice thickness from the advanced microwave scanning radiometer-EOS for coastal polynyas in the Chukchi and Beaufort Seas, IEEE T. Geosci. Remote, 49, 2993–2998, 2011. 2170

TCD
9, 2167–2200, 2015

Tian-Kunze, X., Kaleschke, L., Maaß, N., Mäkynen, M., Serra, N., Drusch, M., and Krumpen, T.: SMOS-derived thin sea ice thickness: algorithm baseline, product specifications and initial verification, The Cryosphere, 8, 997–1018, doi:10.5194/tc-8-997-2014, 2014. 2170

Wadhams, P.: Sea-Ice Topography of the Arctic Ocean in the Region 70° W to 25° E, Philos. T. Roy. Soc. S.-A., 302, 45–85, 1981. 2185, 2186

Wadhams, P., McLaren, A. S., and Weintraub, R.: Ice thickness distribution in Davis Strait in February from submarine sonar profiles, J. Geophys. Res.-Oceans, 90, 1069–1077, 1985. 2185, 2186

Willatt, R., Laxon, S., Giles, K., Cullen, R., Haas, C., and Helm, V.: Ku-band radar penetration into snow cover on Arctic sea ice using airborne data, Ann. Glaciol., 52, 197–205, 2011. 2170

Willmes, S. and Heinemann, G.: Pan-Arctic lead detection from MODIS thermal infrared imagery, Ann. Glaciol., 56, 29–37, 2015. 2169

Wingham, D., Francis, C., Baker, S., Bouzinac, C., Brockley, D., Cullen, R., de Chateau-Thierry, P., Laxon, S., Mallow, U., Mavrocordatos, C., Phalippouc, L., Ratierb, G., Reyc, L., Rostand, F., Viaub, P. and Wallisa, D. W.: CryoSat: A mission to determine the fluctuations in Earth's land and marine ice fields, Adv. Space Res., 37, 841–871, 2006. 2170, 2175

Yu, Y. and Rothrock, D.: Thin ice thickness from satellite thermal imagery, J. Geophys. Res.-Oceans, 101, 25753–25766, 1996. 2170

Zygmuntowska, M., Khvorostovsky, K., Helm, V., and Sandven, S.: Waveform classification of airborne synthetic aperture radar altimeter over Arctic sea ice, The Cryosphere, 7, 1315–1324, doi:10.5194/tc-7-1315-2013, 2013. 2169, 2181, 2182

TCD
9, 2167–2200, 2015

Table 1. Selected classifier performance. The lower three classifiers are derived by (from bottom to top): Ricker et al. (2014), Röhrs et al. (2012) and Laxon et al. (2013). TL: True Leads; FL: False Leads; TI: True Ice; FI: False Ice; TLR and FLR: True and False Lead Rates [%]; eTLR and eFLR: SDs of TLR and FLR within runs [%]. A list of all tested classifier performances is provided as Supplement.

Feat	w	Θ	TL	FL	TI	FI	TLR	FLR	eTLR	eFLR
MAX	10^{-3}	4.28×10^{-10}	10 336	226	576 597	61 841	14.32	0.04	2.07	0.05
MAX	0.5	1.22×10^{-10}	29 435	4220	572 634	42 711	40.80	0.73	3.26	0.24
MAX	1	2.58×10^{-11}	49 204	19 689	557 143	22 964	68.18	3.41	5.89	0.73
MAX TEW	1	2.55×10^{-11} 200	48 808	19 580	557 305	23 307	67.68	3.39	5.61	0.72
PP	0.5	0.425	22 677	7728	569 244	49 351	31.48	1.34	8.62	0.71
PP	1	0.35	46 602	23 623	553 307	25 468	64.66	4.09	4.94	0.66
PP SSD	–	0.18 4	59 809	73 003	504 042	12 146	83.12	12.65	1.40	0.42
MAX	–	6×10^{-10}	6576	00	576 811	65 613	9.11	0.00	1.12	0.00
PP SSD SK PPL PPR	–	0.3125 4 40 40 30	43 875	28 599	548 145	28 381	60.72	4.96	1.74	0.27

TCD
9, 2167–2200, 2015

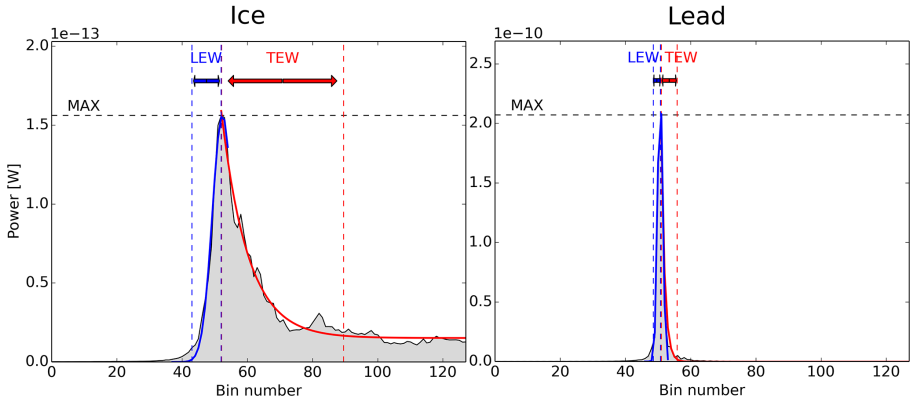

Figure 1. Example CryoSat-2 waveforms from ice (left panel) and a lead (right panel). The definition of the Leading Edge Width (LEW), Trailing Edge Width (TEW) and Maximum Power (MAX) are illustrated while the Pulse Peakiness (PP) is inversely proportional to the gray areas of normalized waveforms. The Bin number can be converted into delay time. Note the different scaling factors of the y axis ($\times 10^{-13}$ and $\times 10^{-10}$ for the ice and lead example, respectively).

TCD
9, 2167–2200, 2015

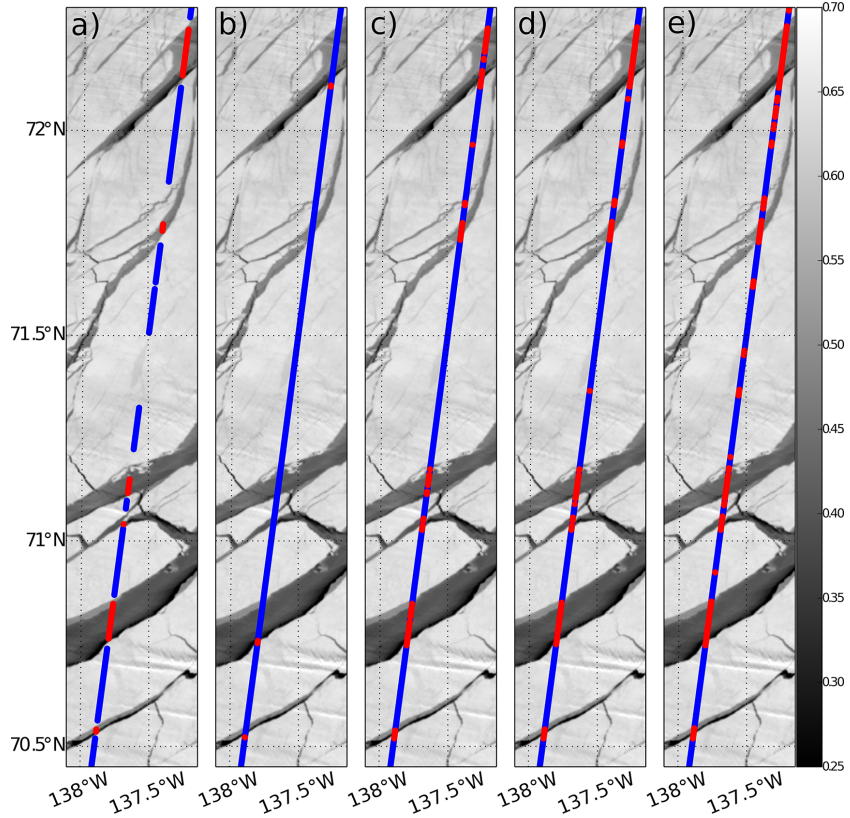

Figure 2. MODIS band 2 scene from 6 March 2013 in the southern Beaufort sea combined with a CS-2 track taken 83 min later on. The CS-2 samples have been classified as lead (red) and ice (blue) manually **(a)** or by the application of thresholds from the **(b)** $MAX_{0.5}$, **(c)** MAX_1, **(d)** Ricker et al. (2014) and **(e)** Laxon et al. (2013) classifier. The classifier from Röhrs et al. (2012) detects no leads within this section.

TCD
9, 2167–2200, 2015

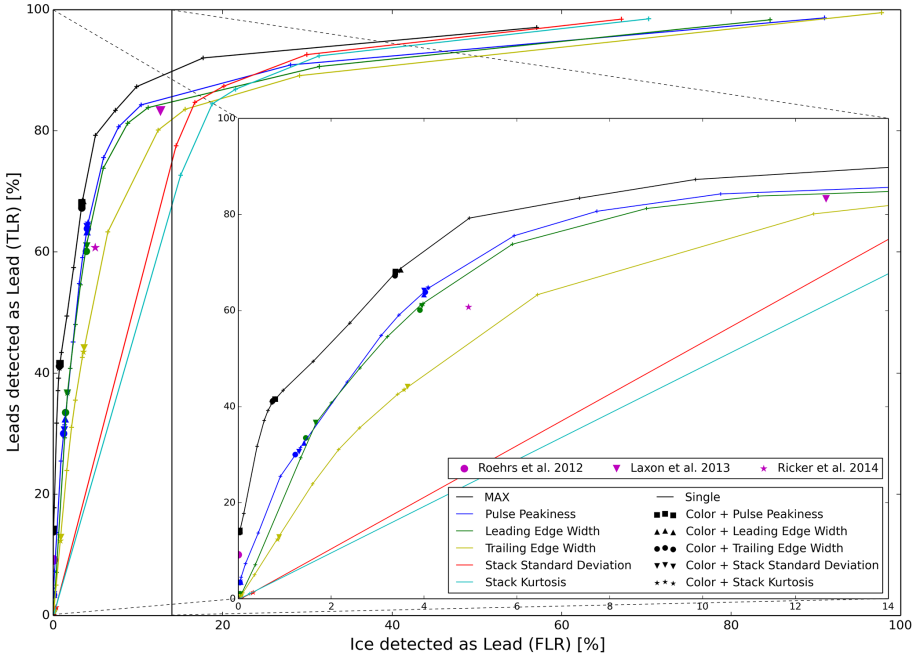

Figure 3. ROC graph of tested classifiers with altering thresholds (**Θ**) on one (connected by lines) and two (marker) parameters as well as predefined classifiers (magenta markers). In the two dimensional case the color indicates one of the parameters and the shape the other one. The insertion is a zoom on small False Lead Rates.

TCD
9, 2167–2200, 2015

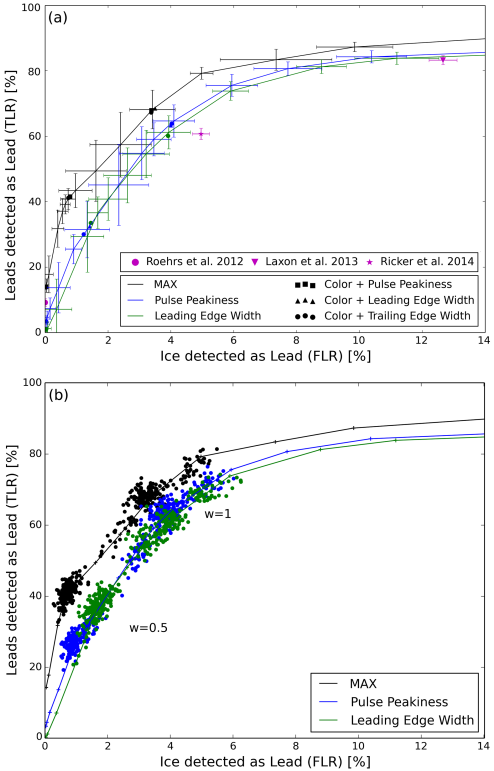

Figure 4. (a) ROC graph including error estimates in terms of SD of the 200 runs for each weight of the single feature classifiers using the MAX, PP and LEW as well as the performances and SDs of the predefined classifiers. For comparison the performances of selected two dimensional classifiers are included. **(b)** Performances of each individual run being part of the single feature classifiers using the MAX, PP and LEW with weights of 0.5 and 1 (dots) in combination with mean values for all weights (lines).

TCD
9, 2167–2200, 2015

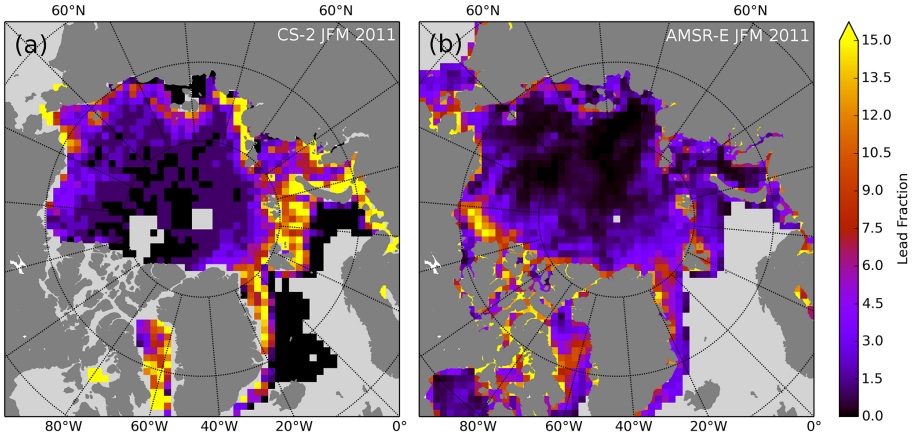

Figure 5. Lead fraction derived from CS-2 SAR-mode **(a)** and from Röhrs et al. (2012) **(b)** on a North Polar Stereographic Grid with a resolution of 99.5 km × 99.5 km, merged from January to March 2011. Only values based on at least 2000 CS-2 measurements north of 65° N **(a)** or with a grid cell data coverage of 10 % or more **(b)** are shown.

TCD
9, 2167–2200, 2015

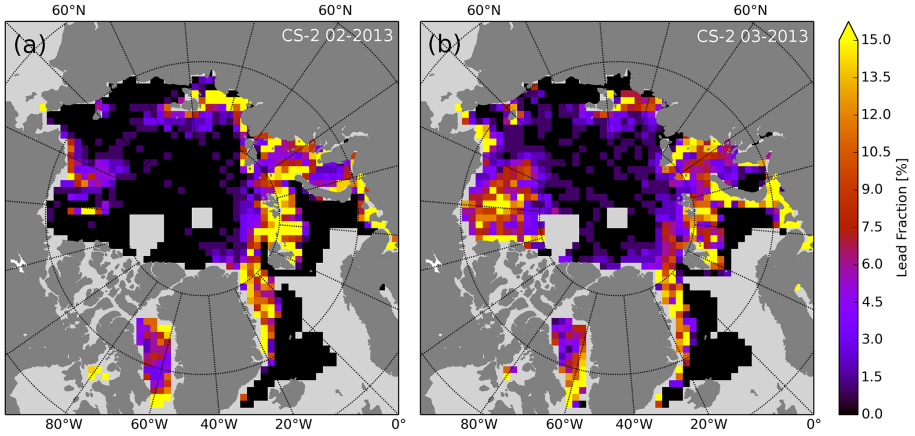

Figure 6. Lead fraction derived from CS-2 SAR-mode on a North Polar Stereographic Grid with a resolution of 99.5 km × 99.5 km from February **(a)** and March 2013 **(b)**. Only lead fraction values north of 65° N based on at least 1000 measurements are shown.

TCD
9, 2167–2200, 2015

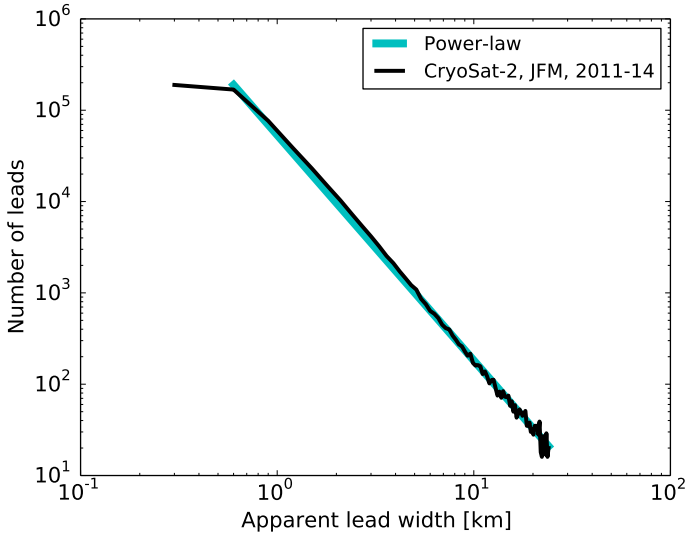

Figure 7. Apparent lead width distribution from all CS-2 SAR-mode ocean measurements north of 65° N in winter season (JFM) from 2011 to 2014. The distribution of a power-law with exponent of 2.47 is included for comparison, forming a straight line in a double logarithmic presentation. See text for definition of the apparent lead width.

TCD
9, 2167–2200, 2015